



Title	Heteroatom-doped porous carbon with tunable pore structure and high specific surface area for high performance supercapacitors
Author(s)	Kim, Cheong; Zhu, Chunyu; Aoki, Yoshitaka; Habazaki, Hiroki
Citation	Electrochimica acta, 314, 173-187 https://doi.org/10.1016/j.electacta.2019.05.074
Issue Date	2019-08-10
Doc URL	http://hdl.handle.net/2115/82437
Rights	© 2019. This manuscript version is made available under the CC-BY-NC-ND 4.0 license http://creativecommons.org/licenses/by-nc-nd/4.0/
Rights(URL)	http://creativecommons.org/licenses/by-nc-nd/4.0/
Type	article (author version)
File Information	Manuscript.pdf



[Instructions for use](#)

Heteroatom-doped porous carbon with tunable pore structure and high specific surface area for high performance supercapacitors

Cheong KIM^a, Chunyu ZHU^{a,b}, Yoshitaka AOKI^{a,b}, Hiroki HABAZAKI^{a,b}*

^a Graduate School of Chemical Sciences and Engineering, Hokkaido University, Sapporo, Hokkaido 060-8628, Japan

^b Division of Applied Chemistry & Frontier Chemistry Center, Faculty of Engineering, Hokkaido University, Sapporo, Hokkaido 060-8628, Japan

Corresponding author: chunyu6zhu@eng.hokudai.ac.jp

Abstract:

Biomass-derived porous carbons with very high specific surface area (SSA) and heteroatom-doping are important for obtaining high performance supercapacitor. In this study, we report a simple and straightforward strategy, which involves the efficient and exothermic pyrolysis of Mg/K/Mg•K-nitrate-urea-cellulose mixture with subsequent high temperature carbonization and washing treatment, to produce N-doped porous carbon with tunable pore structure. The vigorous exothermic pyrolysis of Mg/K/Mg•K-nitrate-urea-cellulose induces the formation of large macropores. The subsequent high temperature carbonization and washing treatments remove Mg,K compounds and facilitate the creation of numerous micro and mesopores. The pore size distribution of the obtained carbon is quite dependent on the Mg•K ratio in the precursors. In this manner, the three-dimensional hierarchical porous carbon with SSA larger than $2700 \text{ m}^2 \text{ g}^{-1}$ is obtained. The obtained porous carbon as the electrodes for supercapacitor in two-electrode measurement shows high specific capacitance (279 F g^{-1} at 1 A g^{-1} in a 6 M KOH electrolyte), excellent cycling stability (larger than 89% capacitance retention after 10,000 cycles at 2 A g^{-1}) and good rate capability (235 F g^{-1} at even 30 A g^{-1}). These results indicate that biomass cellulose-derived heteroatom-doped hierarchical porous carbon is a promising material for supercapacitor.

Keywords: supercapacitor; porous carbon; nitrogen-doping; cellulose; combustion synthesis

1. Introduction

Supercapacitors (SCs), especially for the electrical double layer capacitors (EDLCs), are considered as one of the most promising high-power electrochemical energy devices due to their long cycling stability, high power density, rapid charging/discharging rates, and environmental friendliness. Currently, carbon nanomaterials are the most promising electrode materials for SCs because of their high specific surface area (SSA) and structural diversity. [1, 2] So far, researchers have devoted their efforts to synthesize diverse novel carbon nanostructures for SC applications, for example, carbon nanotubes,[3-5] graphene and their derivatives,[6, 7] porous active carbons [8-12]. To date, the porous activated carbons have been commercially used in SC electrodes due to their advantages such as high specific surface area, the relatively facile production and low cost. The remaining challenges for the porous active carbon-based SCs are their low energy and power density, and the depletion of using fossil-based carbon resources for their production.

The requirement for the depletion of using fossil-based carbon resources for producing porous carbon has motivated researchers to use sustainable biomass, which are abundant, renewable and non-expensive raw materials for carbon. Various biomass raw materials, including lignin, [13, 14] gelatin,[15] starch,[16] wheat and rice straw,[17, 18] plant organs,[19] plane tree fluff, [20] bamboo char, [21] pine tannins,[22] cellulose, [23] etc., have been used to produce porous carbons for SC electrodes with improved capacitive performance. Additionally, the performance of carbon nanomaterials as SC electrodes can be enhanced by several strategies, for example, by increasing the number of active charge sites with enlarged surface area and porosity, and by adding active heteroatoms such as N and S. The first strategy contributes to the enhancement of the electrical double-layer capacitance, while the doping of heteroatoms introduces the additional pseudo-capacitance.[12, 22, 24] It is normally recognized that the

electrochemical capacitive reactions proceed at the electrode and electrolyte interfaces. A hierarchical pore structure containing a multi-porous architecture of interconnected micro (< 2 nm), meso (2 nm ~ 50 nm) and even macropores (> 50 nm) is considered to enhance the capacitive performance, especially the rate capability. The abundant micro and small mesopores offer abundant active sites and large accessible surface areas for the charge accommodation, while the interconnected large meso- and macropores can facilitate the fast ion transport by supplying electrolyte-buffering reservoirs and shortened ion-transport pathways. [9, 25-30] However, the production of porous carbons from biomass raw materials with well-designed pore structure and very high SSA is still challenging. Therefore, the exploration of a facile and efficient method from inexpensive biomass raw materials for producing porous carbons, with heteroatom doping, well-developed hierarchical pore structure and very high SSA, is of great interest for obtaining a superior SC.

Here, in this study, we present a simple and straightforward strategy to produce heteroatom N-doped porous carbon with hierarchical pore structure and very high SSA by using biomass cellulose as the raw material. The pyrolysis of cotton cellulose is carried out in the presence of Mg/K/Mg•K-nitrate and urea under inert atmosphere. This new pyrolysis process is an efficient and vigorous exothermic reaction which is induced by the redox reaction between nitrate oxidant and carbohydrate reductant. The nitrate-assisted exothermic pyrolysis of cellulose proceeds very quickly with the emission of a large amount of gases, which can exfoliate the cellulose micron-fibers to highly porous carbon containing many large meso-macropores. With further high-temperature carbonization and washing treatment to remove the Mg,K compounds, additional micro-mesopores are created. In this manner, the hierarchically interconnected micro-meso-macro porous carbon with very high SSA larger than 2700 m² g⁻¹ and heteroatom N-doping are produced. The effects of carbonization temperature and Mg/K-nitrate ratio in the

precursors on the pore structure, heteroatom doping amount, carbonization degree and their electrochemical capacitive performance are carefully investigated.

2. Experimental section

Preparation of porous carbon: The details for the preparation process are shown in the Supplementary Information (SI). Briefly, in the preparation process, magnesium nitrate hexahydrate and/or potassium nitrate, urea and cotton cellulose are mixed by an impregnation process; subsequently, the mixtures were pyrolyzed and carbonized under Ar atmosphere at high temperatures; finally, after a washing process, porous carbon was obtained. Totally, six samples were produced, which were named based on the molar amount (mmol) of magnesium/potassium nitrates, molar amount (mmol) of urea, mass amount (g) of cotton and carbonization temperature. These samples are Mg10Ur20Cot1g-900, Mg9K2Ur20Cot1g-900, Mg8K4Ur20Cot1g-900, Mg8K4Ur20Cot1g-800, Mg8K4Ur20Cot1g-1000 and K10Ur20Cot1g-900.

The pyrolysis behavior for the nitrate-urea-cotton mixtures were evaluated by a thermogravimetric analyzer combined with a differential thermal analyzer (TG-DTA, NETZSCH STA 2500 Regulus).

Material characterization: The obtained samples were characterized by X-ray diffraction (XRD), scanning/transmission electron microscopy (SEM/TEM), X-ray photoelectron spectroscopy (XPS) and Raman spectrometer. The porous features, including SSA, pore volume and pore size distribution of the samples were characterized by nitrogen adsorption using a

Microtrac-BEL (BELSORP-mini) surface area analyzer. The details for the analysis techniques are shown in the SI.

Electrochemical measurement: The details for the preparation of electrodes and the electrochemical measurement are shown in SI. Briefly, the electrochemical measurement for supercapacitors was conducted using both the symmetric two-electrode cell and the three-electrode half-cell configuration in a 6 M KOH aqueous electrolyte. Cyclic voltammetry (CV), electrochemical impedance spectroscopy (EIS) and galvanostatic charge-discharge measurement were performed.

The specific capacitance based on three-electrode charge-discharge measurement was calculated based on the following formula:

$$C = \frac{I\Delta t}{m\Delta V} \quad (1)$$

where C ($F\ g^{-1}$) is the specific capacitance, I ($A\ g^{-1}$) is current density, Δt (s) is discharge time, m (g) is the mass of a single electrode, and ΔV (V) is the potential window during the discharge process (excluding the IR drop), respectively.

The two-electrode symmetric cell was assembled in a Swagelok-type configuration.[31] The symmetric supercapacitor was tested within a voltage range from 0.0 to 1.0 V. CV and charge-discharge measurement were conducted. The specific capacitance based on two-electrode measurement was calculated based on the following formula:

$$C = \frac{2I\Delta t}{m\Delta V} \quad (2)$$

The energy density (E, Wh kg⁻¹) and power density (P, Wh kg⁻¹) of the two-electrode cells were calculated by using following equations:

$$E = \frac{C(\Delta V)^2}{2 \times 3.6} \quad (3)$$

$$P = \frac{E}{\Delta t} \times 3600 \quad (4)$$

Here C (F g⁻¹) represents the specific capacitance of the supercapacitor calculated from the discharge curves in two-electrode cells. ΔV (V) and Δt (s) refer to the voltage change and the discharge time, respectively.

3. Results and discussion

3.1 The preparation and composition & morphology characterization of porous carbon

Figure 1 presents the schematic diagram for the preparation of heteroatom-doped porous carbon. The metal nitrates and urea were dissolved in water, which were then impregnated into the cotton cellulose. The cotton raw material has the typical hollow cellulose fibers which have length up to several centimeters and diameter of several tens of micrometers, as shown in the inset SEM images in Figure 1. After the impregnation of nitrates and urea, the cotton cellulose can retain their fiber shape. The dried nitrate-urea-cellulose precursors were heated under Ar flow for pyrolysis and carbonization. After carbonization, the samples were washed to remove the potassium and magnesium compounds to produce the final porous carbon products.

The pyrolysis behavior of the nitrate-urea-cellulose precursors were characterized by TG-DTA analysis as shown in Figure 2. It is observed that the pyrolysis of the

nitrate-urea-cellulose are exothermic reactions with sudden weight decreases (Figure 2-(a,b,c)), which occur at around 250 °C for the magnesium nitrate-added samples and at 300 °C for the potassium nitrate-added samples. In addition, the weight decreases lower than around 100 °C in the TG curves were due to the evaporation of absorbed and bonded water. This kind of exothermic reaction is a redox reaction, which is also known as nitrate-introduced combustion synthesis.[32-34] Here, the carbohydrates act as the reductant fuels, while the nitrates are the oxidant. This process is quite different from the endothermic reaction of the direct pyrolysis of pure cellulose, which requires higher decomposition temperature and proceeds slowly, as shown in Figure 2-(d). The exothermic pyrolysis of nitrate-urea-cotton proceeds very fast and efficiently, which can be finished in several minutes when the precursor is ignited. It is also observed that when magnesium nitrate is added, the introduced samples are expanded largely in volume as compared to the only potassium nitrate introduced sample. The use of magnesium nitrate and potassium nitrate makes greatly different pore structure to the final carbon products, which will be discussed in the following sections.

The crystalline features of the samples were evaluated by XRD analysis as shown in Figure 3 and Figure S1 (supplementary information). The typical XRD pattern for the magnesium-potassium nitrate-introduced sample after pyrolysis at 500 °C is shown in Figure 3-(a), which presents the phases of K_2CO_3 , $K_2CO_3 \cdot 1.5H_2O$, KCN, KOCN and MgO. The only magnesium nitrate-introduced sample after pyrolysis at 500 °C (Figure S1-(a)) contains broadened carbon peak (002) and peaks referring to MgO phase, while the only potassium nitrate-introduced sample after pyrolysis at 500 °C (Figure S1-(b)) contains phases of K_2CO_3 , $K_2CO_3 \cdot 1.5H_2O$, KCN and KOCN. Here, the presence of $K_2CO_3 \cdot 1.5H_2O$ phase in the potassium nitrate-introduced samples was due to the reaction of K_2CO_3 with water when the samples were exposed to air. The pre-pyrolyzed precursors were further carbonized at 800-1000 °C, with the

XRD patterns shown in Figure 3-(b) and Figure S1-(c). For the samples treated at 900 and 1000 °C, including Mg10Ur20Cot1g-900, Mg9K2Ur20Cot1g-900, Mg8K4Ur20Cot1g-900, and Mg8K4Ur20Cot1g-1000, a single phase of MgO is observed from the XRD patterns; the XRD peaks for Mg8K4Ur20Cot1g-800 obtained at 800 °C presents multi-phases including MgO, KOCN and KCN; in addition, the carbonized K10Ur20Cot1g-900 presents weak peaks of KCN and $K_2CO_3 \cdot 1.5H_2O$. After washing treatment, the magnesium and potassium species can be easily removed. The XRD patterns for these washed samples in Figure 2-(c,d) present the typical amorphous carbon spectra with greatly broadened peaks at around 23 and 42°, corresponding to carbon (002) and (101), respectively.

SEM and TEM techniques were used for the morphology and microstructure observation of the samples, as shown in Figure 4, Figure 5, Figure S2 and Figure S3. Figure S2 shows the typical SEM images for samples after carbonization. The magnesium nitrate-added samples are highly porous with pores in the range of several tens of nanometers to several hundreds of nanometers; in addition, many nanoparticles of several tens of nanometers according to MgO are observed which are confined in the porous carbon matrix. However, the only potassium nitrate-introduced sample is less porous, and these nanoparticles are not observed. The carbonized samples were finally washed to obtain carbon products. The magnesium nitrate-introduced carbon samples present enhanced porous structure as compared with the only potassium nitrate-introduced one. Figure 4 shows the SEM images of the typical carbon products Mg8K4Ur20Cot1g-900 and K10Ur20Cot1g-900; more images for are shown in Figure S3. From these images, we can confirm that the magnesium nitrate-introduced carbon samples are highly porous, containing pores in a wide range of several nanometers to several hundreds of nanometers; however, the K10Ur20Cot1g-900 carbon is less porous, and only a few big pores of larger than around 100 nm are observed from the SEM images.

The porous structures for Mg8K4Ur20Cot1g-900 and K10Ur20Cot1g-900 were further confirmed by TEM observation in Figure 5. It is observed from the TEM image in Figure 5-(a), sample Mg8K4Ur20Cot1g-900 contains a large number of interconnected mesopores in the range of several tens of nanometers (< 50 nm) and macropores in the range of several tens of nanometers (> 50 nm) to several hundreds of nanometers. The high-resolution image in Figure 5-(b) indicates that the carbon is highly defective with the typical distorted amorphous carbon fringes and the carbon contains numerous small micropores of less than 2 nm. However, the highly interconnected mesopores in the range of several tens of nanometers are not observed for sample K10Ur20Cot1g-900; this sample contains numerous small nanopores of size less than around 4 nm, as shown in Figure 5 (c, d).

3.2 Measurement of the porous characteristics by nitrogen adsorption measurement

The above morphology observation was used to qualitatively observe the porous features of the carbon samples. In this section, nitrogen adsorption measurement was carefully conducted to analyze the porous characteristics. The porous features including SSA, pore volume and pore size distribution of samples were compared. Figure 6 shows the nitrogen adsorption isotherms and the pore size distributions based on non-localized density functional theory (NLDFT) for the final carbon samples. The adsorption curves for the magnesium nitrate-added samples (Mg10Ur20Cot1g-900, Mg9K2Ur20Cot1g-900, Mg8K4Ur20Cot1g-900, Mg8K4Ur20Cot1g-800 and Mg8K4Ur20Cot1g-1000) illustrate the typical hysteresis type isotherms, showing large absorption-desorption hysteresis in relative pressure P/P_0 ranging from ~ 0.5 to 0.8 . This indicates the existence of numerous mesopores. These isotherms also present sharp increases of adsorption at relative pressure of ~ 0.9 – 1.0 , representing the presence of macropores. These isotherms also show steep absorption at P/P_0 near 0, indicating the existence

of many micropores. However, for sample K10Ur20Cot1g-900, the absorption-desorption hysteresis in relative pressure P/P_0 ranging from ~ 0.5 to 0.8 and the steep absorption at relative pressure of ~ 0.9 – 1.0 are very limited, indicating the shortage of mesopores and macropores for this sample. NLDFT pore size distributions of these samples clearly confirm these differences. From Figure 6-(c,d), we can find that the magnesium nitrate-added samples present numerous large mesopores (> 4 nm) and macropores, which were created by the vigorous exothermic pyrolysis with large amount of gas emission and the removal of MgO nanoparticles. These samples also contain a plenty of small nanopores (< 4 nm); the pore ratio in this size range (< 4 nm), especially for the micropores less than 2 nm, is decreased with the increase of magnesium ratio in the Mg/K-nitrates. However, for sample K10Ur20Cot1g-900, the pore distribution is limited to size almost less than 4 nm, and this sample presents a large ratio of pores less than 2 nm. These differences in pore size distribution are caused by the different role of magnesium and potassium compounds, in which magnesium oxide creates pores large than 4 nm while potassium compounds account for the formation of small nanopores less than 4 nm.

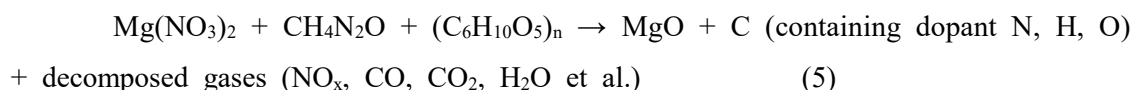
The porous indicators including SSA and pore volumes for the carbon samples are summarized in Table 1. Sample Mg10Ur20Cot1g-900 presents the lowest BET SSA of $1102 \text{ m}^2 \text{ g}^{-1}$. With the addition of potassium precursor, the BET SSA of the samples are greatly increased, which are $2071 \text{ m}^2 \text{ g}^{-1}$ for Mg9K2Ur20Cot1g-900, $2600 \text{ m}^2 \text{ g}^{-1}$ for Mg8K4Ur20Cot1g-900 and $2486 \text{ m}^2 \text{ g}^{-1}$ for K10Ur20Cot1g-900. The pore volumes are also greatly increased for the potassium added samples. The SSA and pore volume of the porous carbons are considered to greatly affect their electrical double layer capacitance.

3.3 Discussion on the pore formation mechanism

Based on the above characterization results, the reactions occurred in the whole process

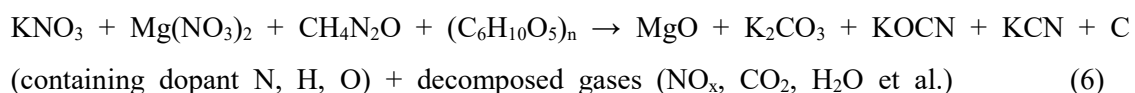
and the pore formation mechanism are discussed in this section.

For the magnesium nitrate-urea-cellulose case, during the pre-pyrolysis process, the following total reaction is proposed to occur:



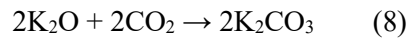
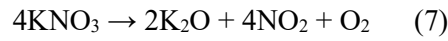
The continuing high-temperature heat treatment induces the further carbonization of amorphous carbon precursor, while MgO phase is dispersed in the carbon matrix showing no phase change during heat treatment, as confirmed by XRD analysis (Figure 3 and Figure S3). During the pre-pyrolysis process, many macropores are formed due to the vigorous exothermic reaction with the emission of large amount of gases. Washing treatment removes the MgO template, creating numerous micro-mesopores in the carbon. Especially, MgO template has the size of several to several tens of nanometers as confirmed by SEM, inducing the formation of numerous mesopores.

When potassium nitrate is also added in the precursors, the involved reactions are much more complex. As evidenced by the previous XRD analysis (Figure 3 and Figure S3), after the pre-pyrolysis, five substances are formed for the Mg•K nitrate-added samples, including the amorphous carbon (containing dopants of N, H, O), MgO, K₂CO₃, KCN and KOCN. The total reaction can be written in the following formula:

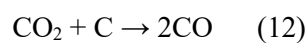
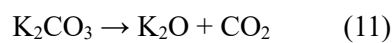


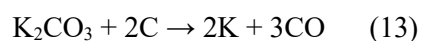
Here, Mg(NO₃)₂ is decomposed to form MgO nanoparticles, which is also stable during the

high-temperature carbonization process, as-evidenced by the XRD analysis. KNO_3 is decomposed and further reacts with the carbohydrate-derived species (CO_2 , HOCN , HCN , H_2O , etc.) to form potassium compounds including K_2CO_3 , KCN and KOCN . Decomposition of cellulose may release CO_2 , H_2O and other C-H gases, while the pyrolysis of urea may release gases such as HOCN , HCN and NH_3 etc.[35, 36] The potassium-included reactions in the pre-pyrolysis step (up to 500 °C) could contain follows:



With further heating to high temperatures for carbonization, the compositions of potassium compounds will change based on the carbonization temperature. At 800 °C, the carbonized sample contains four substances, including carbon, MgO , KCN and KOCN . Here, K_2CO_3 phase disappears, which is decomposed at temperature higher than 700 °C [37] and reacts with the C-N species to form KCN and metallic K. Here, the KCN XRD peak intensity in the 800 °C sample become stronger, while the peaks for KOCN become weaker as compared to the corresponding precursor obtained at 500 °C. The reported decomposition temperature for KOCN is around 700-900 °C. Therefore, the high-temperature activation reactions for the highly porous carbon samples could contain:





In addition, at much higher temperatures of 900 and 1000 °C, potassium species are almost removed due the carbon reduction to form metallic potassium and its evaporation. The evaporation of metallic potassium could make a lot of small cracks in the carbon. It is observed from the XRD patterns that the carbonized samples at 900 and 1000 °C present a small amount potassium-related species. EDS analysis as shown in Figure S4 also confirms the removal of potassium at carbonization temperature higher than 900 °C. Finally, with washing treatment to remove the potassium species and MgO template, abundant micro-mesopores are created in the final carbon sample.

The addition of potassium nitrate in the precursor accounts for the increase of specific surface area and pore volume, especially for the small nanopores (< 4 nm). The potassium compounds act as both template and corrosive agent to carbon for creating small nanopores. This is similar but more complex than the conventional KOH activation process for activated carbons since that the presence of N makes the formation of more complex potassium compounds. [37]

As for the only potassium nitrate-introduced sample, a few macropores larger than 100 nm, as-confirmed by SEM observation, were also created due to the emission of large amount of gases during pyrolysis; the continuing carbonization process at high temperature induced the potassium-based activation process to create numerous nanopores (mainly less than 4 nm). Particularly, the numerous mesopores (> 4 nm) are not contained in this sample.

In summary, the nitrate-induced exothermic reaction is vigorous and fast, which emits a lot of gases that will create many large macropores in the pyrolyzed carbon; the magnesium nitrate addition in the precursor accounts for the formation of a large amount of mesopores (mainly > 4 nm) due to the introduction of MgO nanoparticles with size ranging from several nanometers to several tens of nanometers; the introduced potassium compounds are responsible to the formation of small nanopores less than 4 nm due to the activation effect of potassium species. By controlling the use of magnesium and potassium nitrate, we can obtain a series of porous carbon with tunable pore size distribution and high specific surface area. The as-synthesized porous carbons with typical pore structures are: (1) Mg10Ur20Cot1g-900 has the continuous and interconnected micro-meso-macro hierarchical pores, but the BET SSA is the lowest of 1102 m² g⁻¹; (2) Mg8K4Ur20Cot1g-900 has continuous and interconnected micro-meso-macro hierarchical pores and very high BET SSA of 2600 m² g⁻¹; (3) K10Ur20Cot1g-900 has micro-meso hierarchical nanopores, which are mainly limited to less than 4 nm, and very high SSA of 2486 m² g⁻¹.

3.4 XPS and Raman analysis of the porous carbon

The elemental compositions and bonding features of the carbon materials were measured via XPS. The survey spectra as-shown in Figure 7-(a, e) illustrate the presence of three obvious peaks centered at ~285, 400, and 520 eV, which can be assigned to C1s, N1s, and O1s, respectively. N element is derived from urea. O is the carbonization residue from both cellulose and urea, which is contained in all kinds of activated porous carbon. The N dopant is believed to greatly affect the electrochemical capacitance, which can make additional pseudo-capacitance and increase the wetting of the carbon. The atomic ratios of the N component are summarized in Table 2. The percentage of N dopant is decreased with increasing the heat-treatment temperature

due to the enhanced carbonization and decomposition of N species at higher temperature. The addition of potassium precursor also increases the graphitization of carbon and decreases the amount of N dopant due to the formation of potassium compounds with N and their decomposition/reduction to metallic potassium at high temperatures.

The high-resolution spectra for C 1s and N 1s were also obtained. Figure 7-(b, e) shows the C 1s spectra, which can be separated into three peaks located at around 284.8, 286.2 and 288.5 eV, referring to the C-C or C-H, C-N and/or C-O, and O=C-C bonding, respectively. The narrow scan of the N 1s spectra is shown in Figure 7-(c, f). The deconvolution of the N 1s spectra shows three peaks centered at 398.6, 400.2 and 401.7 eV, corresponding to the pyridinic N, pyrrolic N, and graphitic N, respectively. The ratios for the above three N species are greatly influenced by carbonization temperature and the addition of potassium, which are summarized in Table 2. With the increase of calcination temperature, the samples present increasing ratio of graphitic N, slight decrease of pyridinic N and great decrease of pyrrolic N. With the addition of potassium, the samples show enhanced ratio of graphitic N. These results indicate the enhancement of carbonization with increasing the calcination temperature and adding potassium precursor.

Raman spectra were obtained to further confirm the characteristics of the carbon samples. As shown in Figure S5, all spectra present two peaks located at around 1340 cm^{-1} and 1595 cm^{-1} , corresponding to the disordering structured D-band and ordered sp^2 bonded graphitic G-band, respectively. It is well known that the ratio of the intensity of D-band to G-band (I_D/I_G) is proportional to the disordering degree of the carbon samples. The intensity ratio is summarized in Table 2. At the same calcination temperature of $900\text{ }^\circ\text{C}$, with the addition of potassium precursor, the I_D/I_G ratio decreases from 1.34 for sample Mg10Ur20Cot1g-900 to around 0.99 for K10Ur20Cot1g-900, representing the enhancement of graphitization by the carbon reduction

of potassium compounds to metallic potassium.

3.5 Electrochemical measurement for supercapacitor

The supercapacitor performance of the porous carbons was evaluated in both two-electrode and three-electrode configurations using a 6 M KOH electrolyte.

Figure 8 presents the two-electrode measurement results. Figure 8-(a) shows the typical CV curves for sample Mg8K4Ur20Cot1g-900, which illustrate the symmetrical rectangular shape from 10 to 100 mV s^{-1} , indicating the good double-layer capacitance behavior. The CV curves for other samples are summarized in Figure S6, which also present the symmetrical rectangular shape, excluding sample Mg8K4Ur20Cot1g-800. The CV curves for sample Mg8K4Ur20Cot1g-800 are less rectangular, especially at high scan rate, which is because of its low carbonization degree and more pseudo-capacitance derived from the abundant heteroatom dopants. The galvanostatic charge-discharges curves for all samples were obtained from 1 to 30 A g^{-1} , as shown in Figure 8-(b) and Figure S7. All of the charge-discharge curves, excluding those for sample Mg8K4Ur20Cot1g-800 at the high current density of 30 A g^{-1} , present symmetric triangular shapes, indicating the typical double-layer capacitive behavior of the porous carbon with good reversibility, which agree well with CV measurement. The deformed curves for sample Mg8K4Ur20Cot1g-800 at 30 A g^{-1} is due to its low conductivity since this sample was obtained at a low carbonization temperature.

Figure 8-(c,d) summarizes the gravimetric specific capacitance of the porous carbon at different current densities. Among the three samples carbonized at 900 °C in Figure 8-(c), sample Mg8K4Ur20Cot1g-900 presents the largest capacitances with values of 241 and 195 F g^{-1} at 1 and 30 A g^{-1} , respectively. The greatly increased capacitances for sample Mg8K4Ur20Cot1g-900 is due to its high SSA, N-doping and hierarchical porous structure. As

shown in Figure 8-(d), for the Mg8K4Ur20Cot1g samples carbonized at 800-1000 °C, the one obtained at 800 °C presents the highest capacitances with values of 279 and 235 F g⁻¹ at 1 and 30 A g⁻¹, respectively. Although the SSAs of these three samples are similar, sample Mg8K4Ur20Cot1g-800 shows larger capacitances, which is due to its larger amount of heteroatom dopants, making the increased pseudo-capacitance. To further evaluate the relationship between the pore structure/N-doping content and the SC properties of these samples, the specific capacitances (F m⁻²) are also calculated for the typical samples at current densities of 1 and 30 A g⁻¹, which are summarized in Figure S8. Figure S8-(a) shows the comparison of the samples carbonized at the same temperature of 900 °C. It is noted that the specific capacitance decreases in the following sequence: Mg10Ur20Cot1g-900 > Mg8K4Ur20Cot1g-900 > K10Ur20Cot1g-900. This is mainly caused by N content and pore structure of the carbon samples. Mg10Ur20Cot1g-900 and Mg8K4Ur20Cot1g-900 have similar hierarchical porous structure with interconnected micro-meso-macropores. Although the SSA of Mg8K4Ur20Cot1g-900 is around double of Mg10Ur20Cot1g-900, Mg10Ur20Cot1g-900 has higher specific capacitance which is due to the higher N content of 4.1% for Mg10Ur20Cot1g-900 than 2.0% for Mg8K4Ur20Cot1g-900. The high content of heteroatom dopant can increase the pseudo-capacitance. By comparing sample Mg8K4Ur20Cot1g-900 and K10Ur20Cot1g-900, the SSA of these two samples are similar, however, the specific capacitance is larger for sample Mg8K4Ur20Cot1g-900, which is due to its higher N content and hierarchical pore structure, which is benefit for the efficient use of the charge surface. Figure S8-(b) shows the comparison of specific capacitance for the samples carbonized at different temperatures for samples Mg8K4Ur20Cot1g-800/900/1000. The values of specific capacitance decrease with the increase of carbonization temperature. This is mainly due to the increased pseudo-capacitance for the sample with higher N content which is carbonized at a

lower temperature.

The long cycling test of the samples was conducted under 2 A g^{-1} up to 10,000 cycles, as shown in Figure 8-(e,f). Generally, all samples can present good stability upon cycling with capacity retention efficiency of larger than 89% after 10,000 cycles. Although sample Mg8K4Ur20Cot1g-800 can present relatively higher capacitances in the initial cycles due to the higher heteroatom doping amount as compared with those carbonized at higher temperature, the capacitance of Mg8K4Ur20Cot1g-800 decreases quickly in the initial cycles and stabilizes after around 1000 cycles. The large amount of heteroatom doping for the sample carbonized at lower temperature makes the increase of pseudo-capacitance, however, the low graphitization degree and structure instability induce the quicker capacity decrease upon cycling.

Based on the above discussion with both rate capability and cycling stability, we may conclude that Mg8K4Ur20Cot1g-900 are the best sample with optimal performance. After 10,000 cycles at 2 A g^{-1} , high capacitances of around 225 F g^{-1} can be remained. The good capacitive performance of the heteroatom-doped hierarchical porous carbon obtained in this study is also among the recently reported carbon materials for supercapacitors.[6, 13-15, 21, 27, 29, 38-40]

Three-electrode measurements, including galvanostatic charge/discharge and CV experiments, were also conducted to further confirm the electrochemical performance. The results are summarized in Figure 9, S9 and S10. The same tendency and conclusions can be obtained with the two-electrode measurement results. Generally, the gravimetric capacitances obtained from three-electrode tests are higher than those calculated from two-electrode measurement, which is normally found in three-electrode measurement due to the possible additional pseudo-capacitances. [41] The capacitance contribution of pure nickel foam in alkaline solution especially for pseudo-capacitor tests is usually considered to be

non-negligible.

EIS was also carried out to evaluate the electrochemical behavior of the electrodes. Figure 10 shows the Nyquist plots of the typical samples in three-electrode configuration. Theoretically, the Nyquist plot for a supercapacitor consists of a high-frequency semicircular arc and a low-frequency straight line.[17, 24] The straight lines in the low frequency region are related to capacitive performance, and the steep lines suggest that the electro-sorption of ions at the interface is not limited by the diffusion process, revealing the excellent behavior of supercapacitors of the prepared carbon samples. The diameters of the semicircles represent the charge transfer resistances (R_{ct}). All plots show small semicircles (with diameters less than 1 ohm), indicating the fast ion transport between the electrodes and the electrolyte. The horizontal axis intercept in the high frequency region of the Nyquist plot is called the equivalent series resistance (R_s), which contains the electrolyte resistance, the intrinsic resistance of the active electrode materials, and the contact resistance at the interface between the current collector. The R_s is at around 0.6 ohm for these electrodes, indicating the good contact and electrolyte conduction of these electrodes. The equivalent circuit is simulated, which is consisted of R_s , R_{ct} , constant phase element (CPE) and Warburg resistance (W_s). The slope of the 45° portion of the curve at intermediate-frequency is W_s , which is a result of frequency dependence of ion diffusion/transport in the electrolyte to the electrode surface. These values are summarized in Table S1. By comparing the plots of K10Ur20Cot1g-900 and Mg8K4Ur20Cot1g-900 in Figure 10-(a), the R_{ct} for Mg8K4Ur20Cot1g-900 is smaller than K10Ur20Cot1g-900. This is due to the containing of much more open and large pores for sample Mg8K4Ur20Cot1g-900, which is beneficial to a faster ion transport in the hierarchical porous structure. Figure 10-(b) presents the comparison of the Nyquist plots for the samples obtained under different carbonization temperatures. The R_s and W_s values are similar, however, R_{ct} is lower for the samples obtained

at higher carbonization temperature (0.63, 0.41 and 0.38 Ω for samples obtained at 800, 900 and 1000, respectively). indicating the increasing electron and ion conduction for the highly graphited samples obtained at a higher carbonization temperature. Another feature is the straight line at low frequency. Normally, it is well known that W_s is related to the distributed electronic and ionic conductivity and double-layer capacitance inside the micropores.[42] Figure S11-(b) shows the Nyquist plots with low frequency region of the Mg8K4Ur20Cot1g samples obtained at different carbonization temperatures. Mg8K4Ur20Cot1g-900 and Mg8K4Ur20Cot1g-1000 show the lower Warburg impedance until 0.25 Hz compared to Mg8K4Ur20Cot1g-800. Moreover, Mg8K4Ur20Cot1g-900 and Mg8K4Ur20Cot1g-1000 increase the angle of the slope at low frequency (0.25 Hz to 0.05 Hz), indicating that the double-layer capacitance will be increased compared to Mg8K4Ur20Cot1g-800. Figure 11-(c) shows the bode plots of Mg8K4Ur20Cot1g samples, which can be clearly distinguished by the high, middle and low frequency regions. The phase angle at the low frequency region (~ 1 Hz) indicates capacitive behavior. It is known that the phase angle towards -90° attributes the better capacitor behavior.[43] The phase angles of Mg8K4Ur20Cot1g-900 and Mg8K4Ur20Cot1g-1000 are -71° and -70° , respectively, which are closer to -90° than Mg8K4Ur20Cot1g-800 with a value of -54° .

Finally, Figure 11 shows the Ragone plots of the typical symmetric cells, in comparison with the previously reported porous carbons (as summarized in Table S2). The supercapacitor can deliver a high energy density of 38.7 Wh kg^{-1} and the power density is up to 45.3 kW kg^{-1} based on the active materials, which is among the highest values as compared with the reported porous carbons.

The outstanding supercapacitor performance in terms of high capacitance, good cycling

stability and superior rate capacity obtained in this work are ascribed to the very high surface area, heteroatom doping and hierarchical micro-meso-macro-porous structure. The very high SSA of the porous carbon offers a large number of active sites for ion absorption/desorption. The heteroatom doping with N element provides additional pseudo-capacitance to the overall capacitance and enhances the wettability of the electrode materials to facilitate the easy accesses of the electrolyte ions. The hierarchical pore structure with interconnected micro-meso or even macropores can not only accommodate high accessibility of electrons and ions, but also provide a path for the fast ion diffusion into the interior micropores. These characteristics of the porous carbon play cooperative effects on enhancing the electrochemical performance. Importantly, the heteroatom-doped porous carbon with well-developed hierarchical pore structure can be facilely prepared by an efficient exothermic pyrolysis process with subsequent high temperature carbonization and washing treatment by using the sustainable carbon source of biomass cellulose.

4 Conclusions

In summary, we efficiently synthesized the heteroatom doped hierarchical porous carbon by using biomass cellulose as carbon source. By involving the vigorous exothermic pyrolysis of the Mg/(K)-nitrate-urea-cellulose mixture, meso-macropores were created in the cellulose-derived carbon. After being further carbonized at high temperature and washed, additional numerous micro-mesopores were formed by removing the Mg,K compounds that were dispersed in the carbon matrix. Finally, the hierarchically interconnected micro-meso-macro-porous carbons with very high BET specific surface area larger than 2700 m² g⁻¹ were produced. The addition of potassium nitrate in the raw materials could greatly

increase the SSA to larger than $2000 \text{ m}^2 \text{ g}^{-1}$, as compared to the magnesium nitrate added sample with SSA of around $1100 \text{ m}^2 \text{ g}^{-1}$. This was due to the activation effect of potassium in creating numerous small micro-mesopores. The obtained porous carbons presented good capacitive performance as the electrodes in supercapacitors, due to their advantageous characteristics including high surface area, hierarchical pore structure and heteroatom doping. In the two-electrode symmetric measurement, the heteroatom-doped hierarchical porous carbons showed high specific capacitance of 279 F g^{-1} at 1 A g^{-1} in a 6 M KOH electrolyte, excellent cycling stability ($> 89\%$ capacitance retention after 10,000 cycles at 2 A g^{-1}) and good rate capability (235 F g^{-1} at even 30 A g^{-1}). The facile production and outstanding electrochemical performance of the heteroatom doped hierarchical porous carbons reinforced their promising application in supercapacitors, which may also find potential applications in the fields of gas storage, catalysis and pollutant absorbent.

Acknowledgements: This work was supported by JSPS KAKENHI Grant Number 18K14047. The authors also thank the “Nanotechnology platform” Program of the Ministry of Education, Culture, Sports, Science and Technology (MEXT) for the use of analysis equipment. This work was also supported partially by “2018 Feasibility Study Program of the Frontier Chemistry Center, Faculty of Engineering, Hokkaido University”.

References

- [1] M.R. Benzigar, S.N. Talapaneni, S. Joseph, K. Ramadass, G. Singh, J. Scaranto, U. Ravon, K. Al-Bahily, A. Vinu, Recent advances in functionalized micro and mesoporous carbon materials: synthesis and applications, *Chemical Society Reviews* 47 (2018) 2680-2721.
- [2] T.Y. Liu, F. Zhang, Y. Song, Y. Li, Revitalizing carbon supercapacitor electrodes with hierarchical porous structures, *Journal of Materials Chemistry A* 5 (2017) 17705-17733.
- [3] D.-Z. Chen, J. Yu, W. Lu, Y. Zhao, Y. Yan, T.-W. Chou, Temperature effects on electrochemical performance of carbon nanotube film based flexible all-solid-state supercapacitors, *Electrochimica Acta* 233 (2017) 181-189.
- [4] Y. Zhang, T. Mao, H. Wu, L. Cheng, L. Zheng, Carbon Nanotubes Grown on Flax Fabric as Hierarchical All-Carbon Flexible Electrodes for Supercapacitors, *Advanced Materials Interfaces* 4 (2017) 1601123.
- [5] E.A. Nagelli, L. Huang, A.Q.-Z. Dai, F. Du, L. Dai, 3D Vertically Aligned CNT/Graphene Hybrids from Layer-by-Layer Transfer for Supercapacitors, *Particle & Particle Systems Characterization* 34 (2017) 1700131.
- [6] I.L. Tsai, J. Cao, L. Le Fevre, B. Wang, R. Todd, R.A.W. Dryfe, A.J. Forsyth, Graphene-enhanced electrodes for scalable supercapacitors, *Electrochimica Acta* 257 (2017) 372-379.
- [7] J. Li, J. Tang, J. Yuan, K. Zhang, Y. Sun, H. Zhang, L.-C. Qin, Enlarging energy density of supercapacitors using unequal graphene electrodes and ionic liquid electrolyte, *Electrochimica Acta* 258 (2017) 1053-1058.
- [8] Y.Y. Smolin, K.L. Van Aken, M. Boota, M. Soroush, Y. Gogotsi, K.K.S. Lau, Engineering Ultrathin Polyaniline in Micro/Mesoporous Carbon Supercapacitor Electrodes Using Oxidative Chemical Vapor Deposition, *Advanced Materials Interfaces* 4 (2017) 1601201.
- [9] J.W. Jeon, J.H. Han, S.-K. Kim, D.-G. Kim, Y.S. Kim, D.H. Suh, Y.T. Hong, T.-H. Kim, B.G. Kim, Intrinsically microporous polymer-based hierarchical nanostructuring of electrodes via nonsolvent-induced phase separation for high-performance supercapacitors, *Journal of Materials Chemistry A* 6 (2018) 8909-8915.
- [10] Y. Wang, L. Jiang, Roles of Graphene Oxide in Hydrothermal Carbonization and Microwave Irradiation of Distiller's Dried Grains with Solubles To Produce Supercapacitor Electrodes, *ACS Sustainable Chemistry & Engineering* 5 (2017) 5588-5597.
- [11] W. Gao, D. Chen, H. Quan, R. Zou, W. Wang, X. Luo, L. Guo, Fabrication of Hierarchical Porous Metal-Organic Framework Electrode for Aqueous Asymmetric Supercapacitor, *ACS Sustainable Chemistry & Engineering* 5 (2017) 4144-4153.
- [12] L. Miao, H. Duan, M. Liu, W. Lu, D. Zhu, T. Chen, L. Li, L. Gan, Poly(ionic liquid)-derived, N, S-codoped ultramicroporous carbon nanoparticles for supercapacitors, *Chemical Engineering Journal* 317 (2017) 651-659.
- [13] W. Zhang, C. Yu, L. Chang, W. Zhong, W. Yang, Three-dimensional nitrogen-doped hierarchical

porous carbon derived from cross-linked lignin derivatives for high performance supercapacitors, *Electrochimica Acta* 282 (2018) 642-652.

[14] J. Pang, W. Zhang, J. Zhang, G. Cao, M. Han, Y. Yang, Facile and sustainable synthesis of sodium lignosulfonate derived hierarchical porous carbons for supercapacitors with high volumetric energy densities, *Green Chemistry* 19 (2017) 3916-3926.

[15] H. Fan, W. Shen, Gelatin-Based Microporous Carbon Nanosheets as High Performance Supercapacitor Electrodes, *ACS Sustainable Chemistry & Engineering* 4 (2016) 1328-1337.

[16] Y. Zhong, T. Shi, Y. Huang, S. Cheng, G. Liao, Z. Tang, One-step synthesis of porous carbon derived from starch for all-carbon binder-free high-rate supercapacitor, *Electrochimica Acta* 269 (2018) 676-685.

[17] S. Zhang, K. Tian, B.-H. Cheng, H. Jiang, Preparation of N-Doped Supercapacitor Materials by Integrated Salt Templating and Silicon Hard Templating by Pyrolysis of Biomass Wastes, *ACS Sustainable Chemistry & Engineering* 5 (2017) 6682-6691.

[18] Z. Chen, H. Zhuo, Y. Hu, L. Zhong, X. Peng, S. Jing, Q. Liu, X. Zhang, C. Liu, R. Sun, Self-Biotemplate Preparation of Hierarchical Porous Carbon with Rational Mesopore Ratio and High Oxygen Content for an Ultrahigh Energy-Density Supercapacitor, *ACS Sustainable Chemistry & Engineering* 6 (2018) 7138-7150.

[19] Y. Zhang, S. Liu, X. Zheng, X. Wang, Y. Xu, H. Tang, F. Kang, Q.-H. Yang, J. Luo, Biomass Organs Control the Porosity of Their Pyrolyzed Carbon, *Advanced Functional Materials* 27 (2017) 1604687-n/a.

[20] Y. Zhang, X. Liu, S. Wang, S. Dou, L. Li, Interconnected honeycomb-like porous carbon derived from plane tree fluff for high performance supercapacitors, *Journal of Materials Chemistry A* 4 (2016) 10869-10877.

[21] Y. Gong, D. Li, C. Luo, Q. Fu, C. Pan, Highly porous graphitic biomass carbon as advanced electrode materials for supercapacitors, *Green Chemistry* 19 (2017) 4132-4140.

[22] A. Sanchez-Sanchez, M.T. Izquierdo, S. Mathieu, J. González-Álvarez, A. Celzard, V. Fierro, Outstanding electrochemical performance of highly N- and O-doped carbons derived from pine tannin, *Green Chemistry* 19 (2017) 2653-2665.

[23] Y. Hu, X. Tong, H. Zhuo, L. Zhong, X. Peng, S. Wang, R. Sun, 3D hierarchical porous N-doped carbon aerogel from renewable cellulose: an attractive carbon for high-performance supercapacitor electrodes and CO₂ adsorption, *RSC Advances* 6 (2016) 15788-15795.

[24] Z. Song, L. Li, D. Zhu, L. Miao, H. Duan, Z. Wang, W. Xiong, Y. Lv, M. Liu, L. Gan, Synergistic design of a N, O co-doped honeycomb carbon electrode and an ionogel electrolyte enabling all-solid-state supercapacitors with an ultrahigh energy density, *Journal of Materials Chemistry A* 7 (2019) 816-826.

[25] J. Wang, J. Tang, B. Ding, V. Malgras, Z. Chang, X. Hao, Y. Wang, H. Dou, X. Zhang, Y. Yamauchi, Hierarchical porous carbons with layer-by-layer motif architectures from confined soft-template self-assembly in layered materials, *Nature Communications* 8 (2017) 15717.

[26] D. Jia, X. Yu, H. Tan, X. Li, F. Han, L. Li, H. Liu, Hierarchical porous carbon with ordered straight

micro-channels templated by continuous filament glass fiber arrays for high performance supercapacitors, *Journal of Materials Chemistry A* 5 (2017) 1516-1525.

[27] Y. Cai, Y. Luo, H. Dong, X. Zhao, Y. Xiao, Y. Liang, H. Hu, Y. Liu, M. Zheng, Hierarchically porous carbon nanosheets derived from *Moringa oleifera* stems as electrode material for high-performance electric double-layer capacitors, *Journal of Power Sources* 353 (2017) 260-269.

[28] L.-N. Han, X. Wei, Q.-C. Zhu, S.-M. Xu, K.-X. Wang, J.-S. Chen, Nitrogen-doped carbon nets with micro/mesoporous structures as electrodes for high-performance supercapacitors, *Journal of Materials Chemistry A* 4 (2016) 16698-16705.

[29] L. Zhou, H. Cao, S. Zhu, L. Hou, C. Yuan, Hierarchical micro-/mesoporous N- and O-enriched carbon derived from disposable cashmere: a competitive cost-effective material for high-performance electrochemical capacitors, *Green Chemistry* 17 (2015) 2373-2382.

[30] H. Su, H. Zhang, F. Liu, F. Chun, B. Zhang, X. Chu, H. Huang, W. Deng, B. Gu, H. Zhang, X. Zheng, M. Zhu, W. Yang, High power supercapacitors based on hierarchically porous sheet-like nanocarbons with ionic liquid electrolytes, *Chemical Engineering Journal* 322 (2017) 73-81.

[31] C. Zhu, G. Saito, T. Akiyama, A new CaCO_3 -template method to synthesize nanoporous manganese oxide hollow structures and their transformation to high-performance LiMn_2O_4 cathodes for lithium-ion batteries, *Journal of Materials Chemistry A* 1 (2013) 7077-7082.

[32] C. Zhu, M. Takata, Y. Aoki, H. Habazaki, Nitrogen-doped porous carbon as-mediated by a facile solution combustion synthesis for supercapacitor and oxygen reduction electrocatalyst, *Chemical Engineering Journal* 350 (2018) 278-289.

[33] C. Zhu, A. Nobuta, I. Nakatsugawa, T. Akiyama, Solution combustion synthesis of LaMO_3 ($M = \text{Fe}, \text{Co}, \text{Mn}$) perovskite nanoparticles and the measurement of their electrocatalytic properties for air cathode, *International Journal of Hydrogen Energy* 38 (2013) 13238-13248.

[34] F. Deganello, A.K. Tyagi, Solution combustion synthesis, energy and environment: Best parameters for better materials, *Progress in Crystal Growth and Characterization of Materials* 64 (2018) 23-61.

[35] N. Tsubouchi, M. Nishio, Y. Mochizuki, Role of nitrogen in pore development in activated carbon prepared by potassium carbonate activation of lignin, *Applied Surface Science* 371 (2016) 301-306.

[36] P.M. Schaber, J. Colson, S. Higgins, D. Thielen, B. Anspach, J. Brauer, Thermal decomposition (pyrolysis) of urea in an open reaction vessel, *Thermochimica Acta* 424 (2004) 131-142.

[37] J. Wang, S. Kaskel, KOH activation of carbon-based materials for energy storage, *Journal of Materials Chemistry* 22 (2012) 23710-23725.

[38] Z. Ling, Z. Wang, M. Zhang, C. Yu, G. Wang, Y. Dong, S. Liu, Y. Wang, J. Qiu, Sustainable Synthesis and Assembly of Biomass-Derived B/N Co-Doped Carbon Nanosheets with Ultrahigh Aspect Ratio for High-Performance Supercapacitors, *Advanced Functional Materials* 26 (2016) 111-119.

[39] X. Wei, Y. Li, S. Gao, Biomass-derived interconnected carbon nanoring electrochemical capacitors with high performance in both strongly acidic and alkaline electrolytes, *Journal of Materials Chemistry A*

5 (2017) 181-188.

[40] H. Feng, H. Hu, H. Dong, Y. Xiao, Y. Cai, B. Lei, Y. Liu, M. Zheng, Hierarchical structured carbon derived from bagasse wastes: A simple and efficient synthesis route and its improved electrochemical properties for high-performance supercapacitors, *Journal of Power Sources* 302 (2016) 164-173.

[41] Z. Liu, Y. Zeng, Q. Tang, A. Hu, K. Xiao, S. Zhang, W. Deng, B. Fan, Y. Zhu, X. Chen, Potassium vapor assisted preparation of highly graphitized hierarchical porous carbon for high rate performance supercapacitors, *Journal of Power Sources* 361 (2017) 70-79.

[42] A. Di Fabio, A. Giorgi, M. Mastragostino, F. Soavi Carbon-Poly(3-methylthiophene) Hybrid Supercapacitors, *Journal of The Electrochemical Society* 148 (2001) A845-A850.

[43] S.K. Jana, B. Saha, B. Satpati, S. Banerjee, Structural and electrochemical analysis of a novel co-electrodeposited Mn₂O₃-Au nanocomposite thin film, *Dalton Transactions* 44 (2015) 9158-9169.

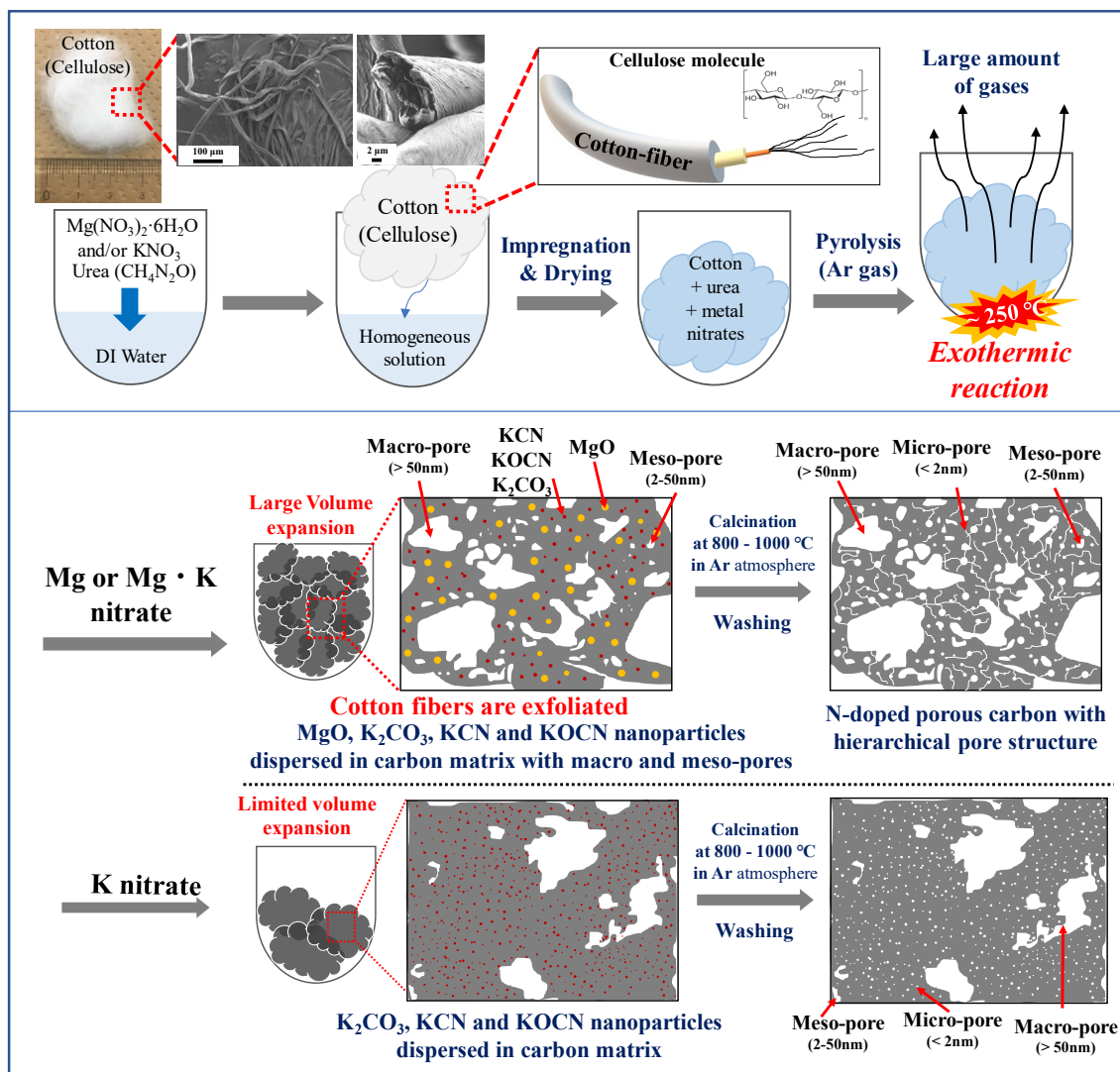


Figure 1. Schematic diagram for the preparation of heteroatom-doped porous carbon with different hierarchical pore structures.

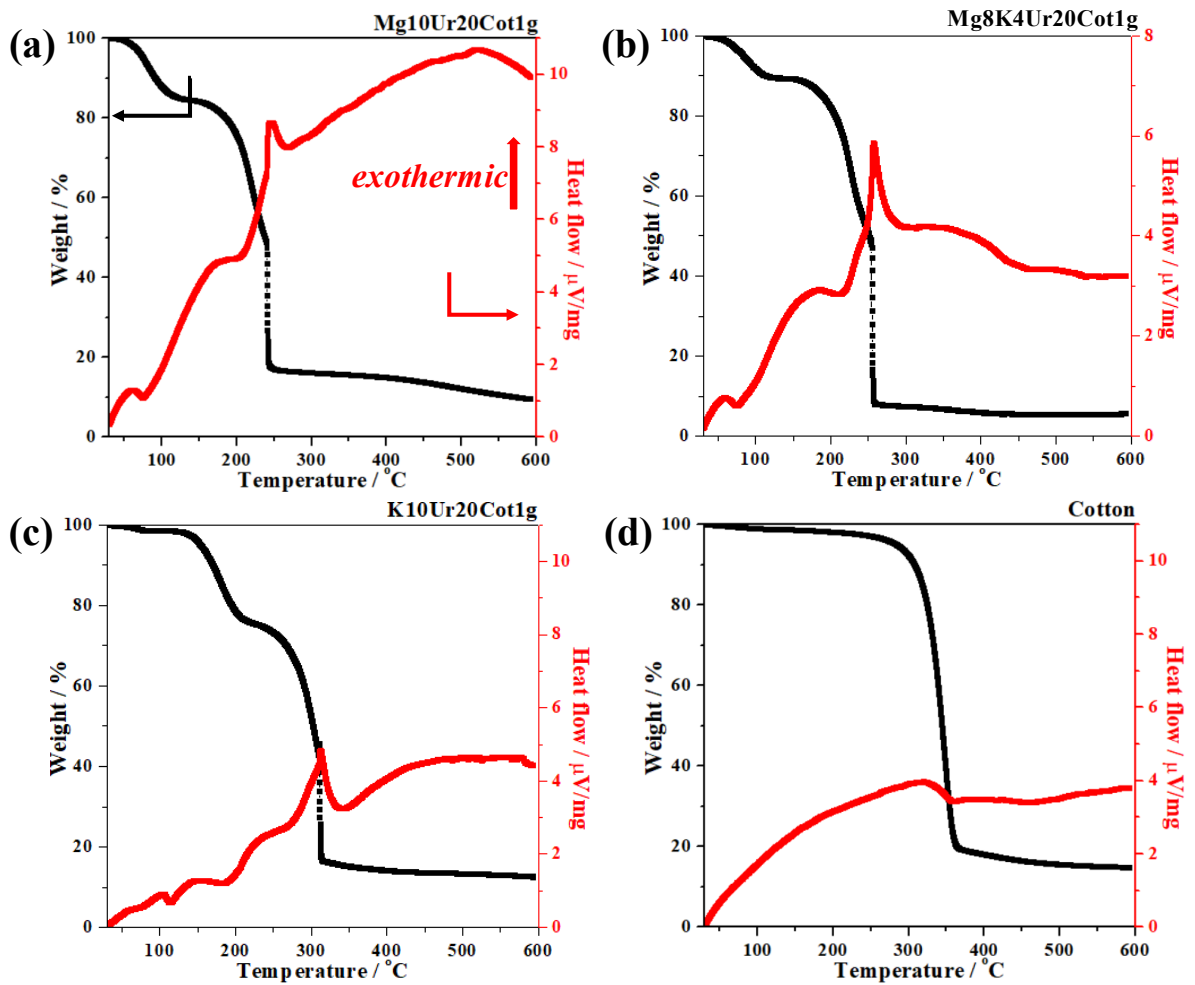


Figure 2. TG-DTA curves of the pyrolysis behavior of different precursors. (a) Mg10Ur20Cot1g; (b) Mg8K4Ur20Cot1g; (c) K10Ur20Cot1g; and (d) only cotton.

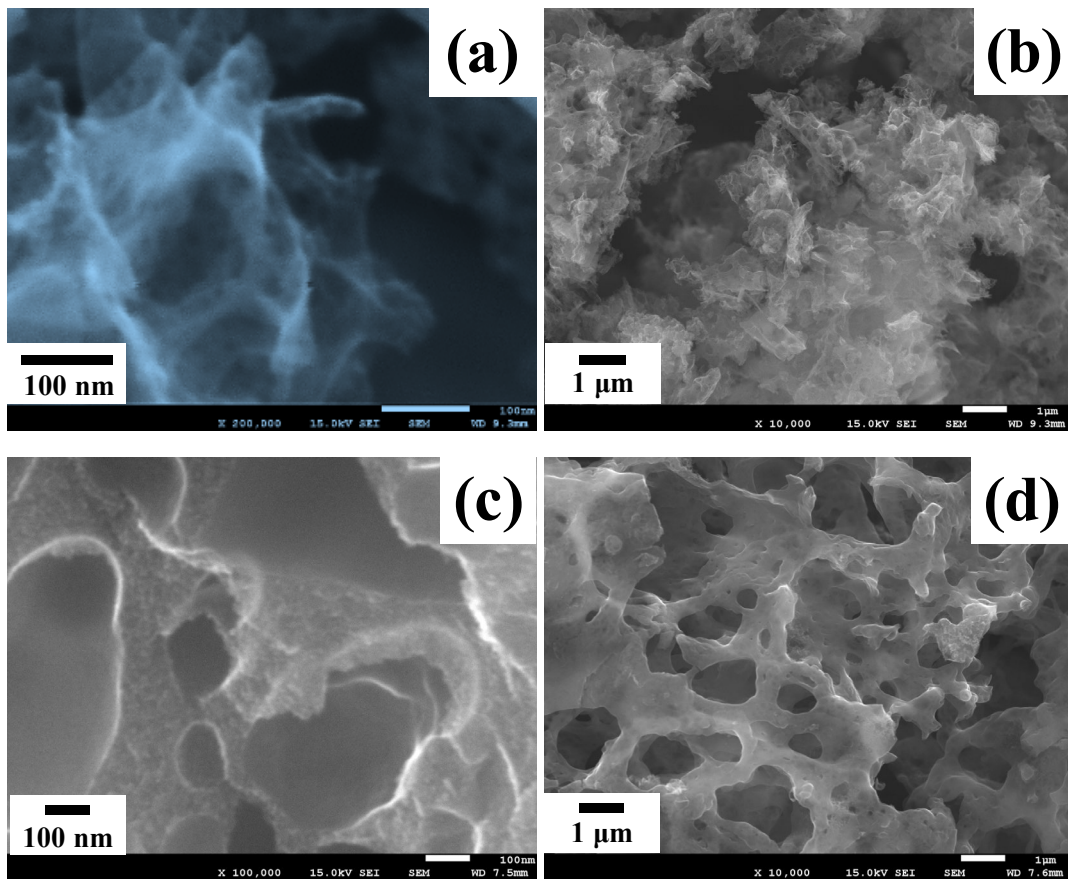


Figure 4. SEM images of the typical samples. (a, b) SEM images of sample Mg8K4Ur20Cot1g-900 after washing; (c, d) SEM images for K10Ur20Cot1g-900 after washing. More images of the obtained samples are shown in the supporting information.

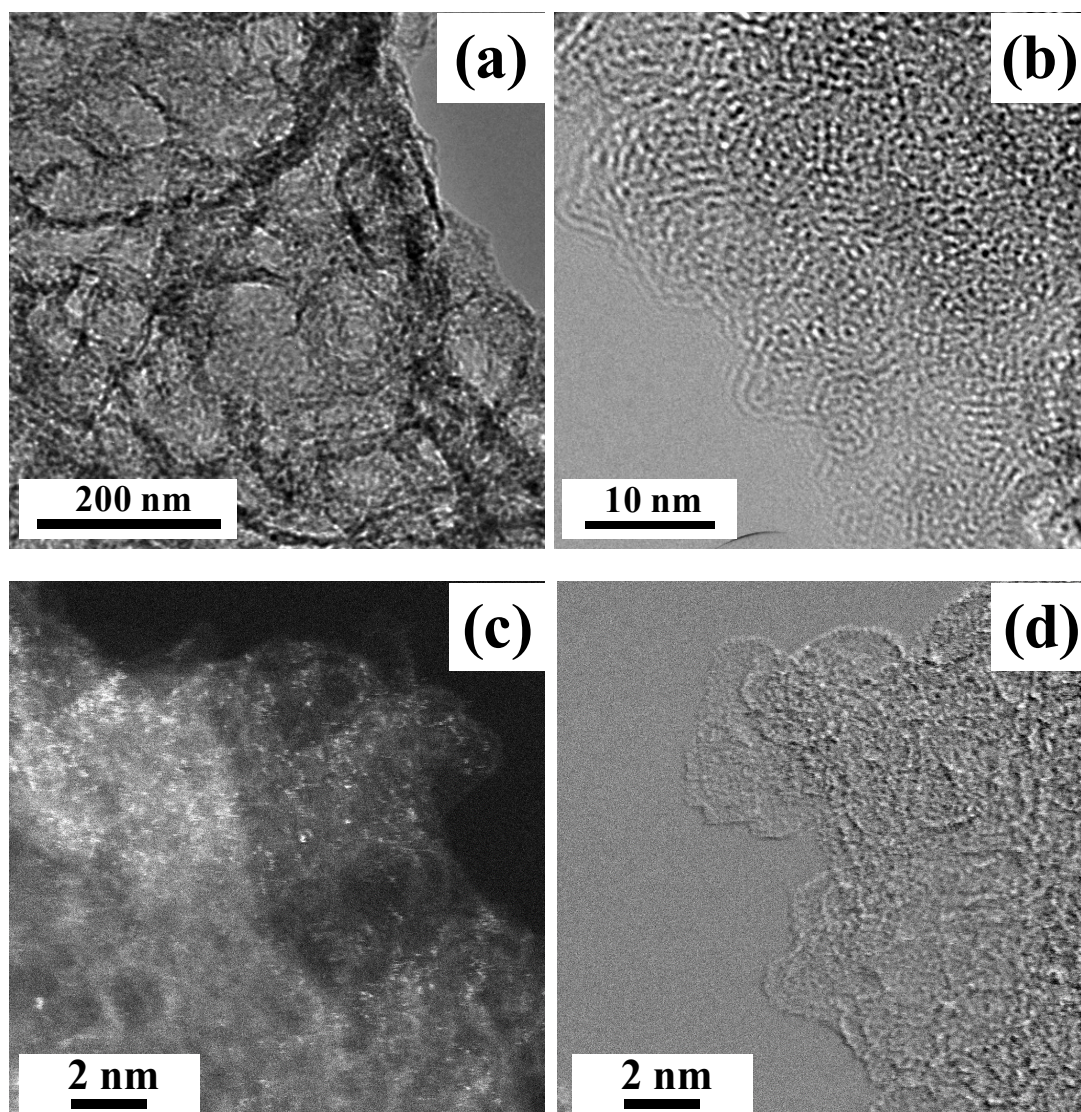


Figure 5. TEM observation results of the typical samples. (a, b) sample Mg₈K₄Ur₂₀Cot₁g-900 after washing; (c, d) K₁₀Ur₂₀Cot₁g-900 after washing.

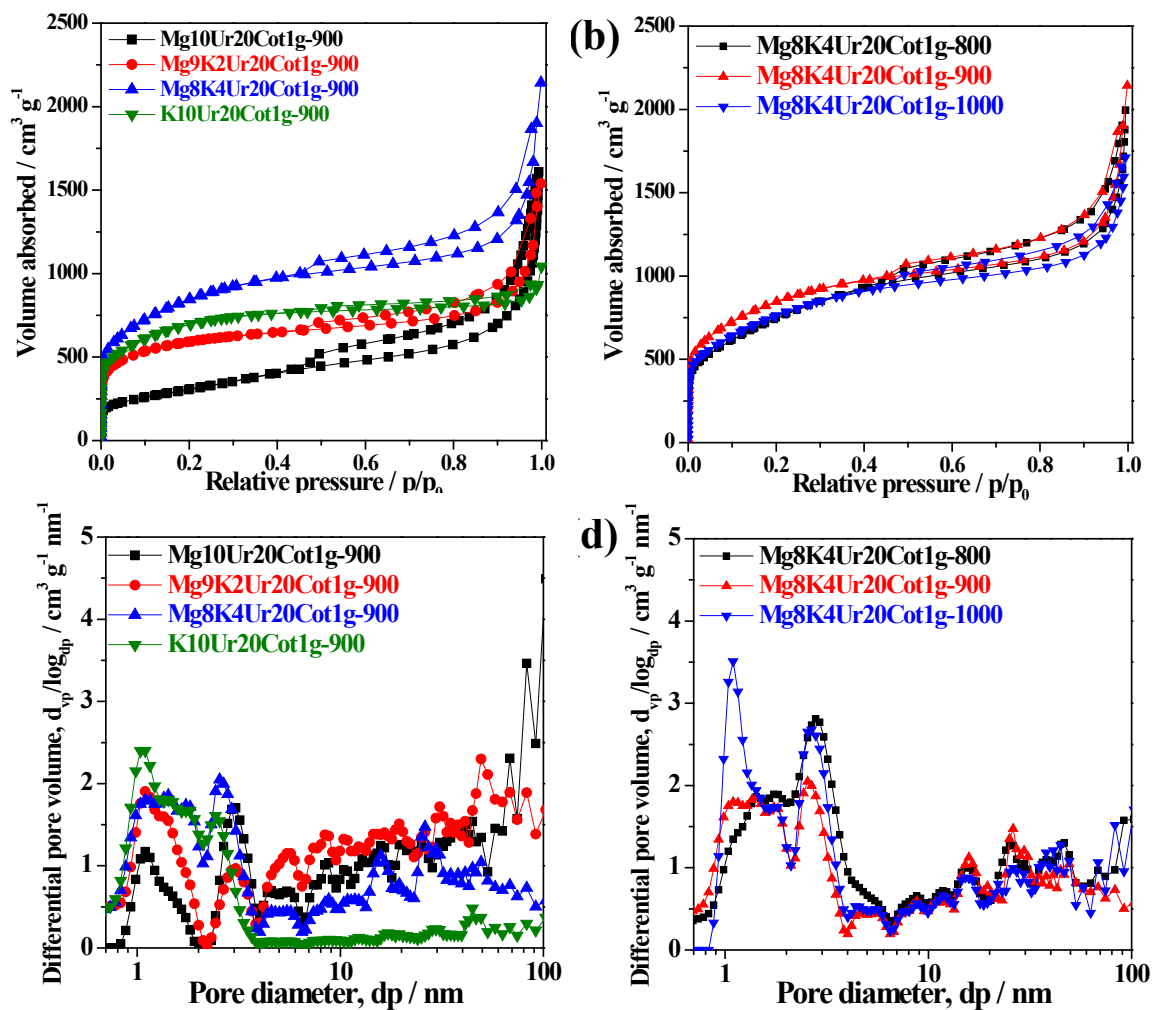


Figure 6. Nitrogen adsorption isotherm (a, b) NLDFT pore size distribution (c, d) for the final carbon samples obtained after washing treatment.

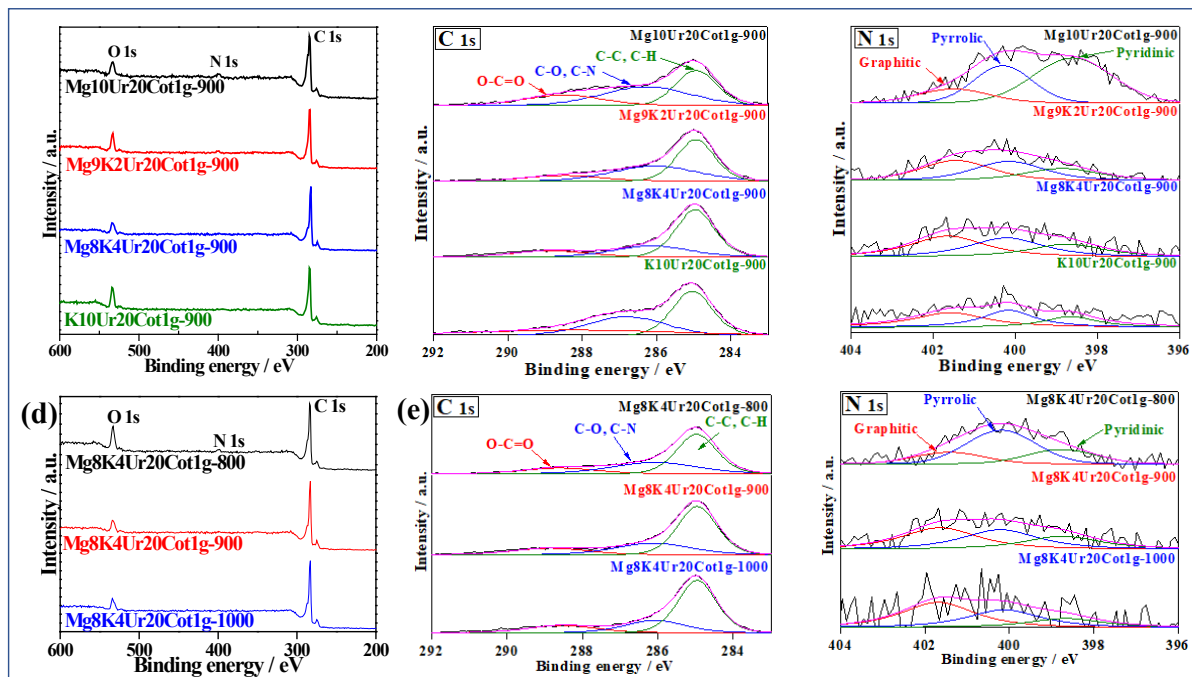


Figure 7. XPS analysis of the obtained carbon samples. (a, d) the wide scan; (b, e) the narrow scan of C1s; (c, f) the narrow scan of N1s.

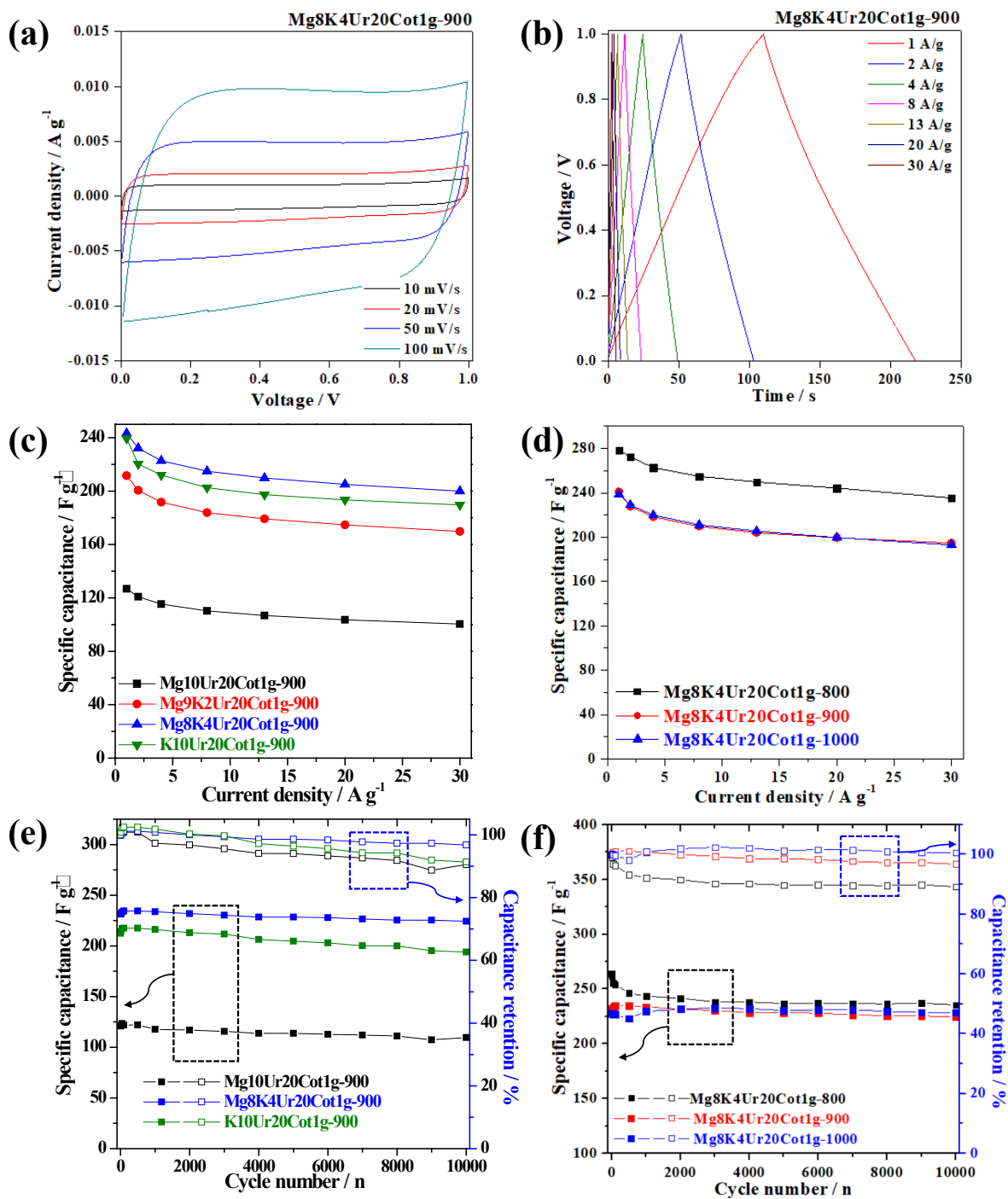


Figure 8. Two-electrode test of the supercapacitors in 6 mol L⁻¹ KOH. (a) Cyclic voltammogram curves of the Mg8K4Ur20Cot1g-900 at various scan rates. (b) Galvanostatic charge-discharge curves of Mg8K4Ur20Cot1g-900 under various current densities. (c, d) Specific capacitance at various current density. (e, f) Long cycle stability in 10000 cycles at a current density of 2 A g⁻¹.

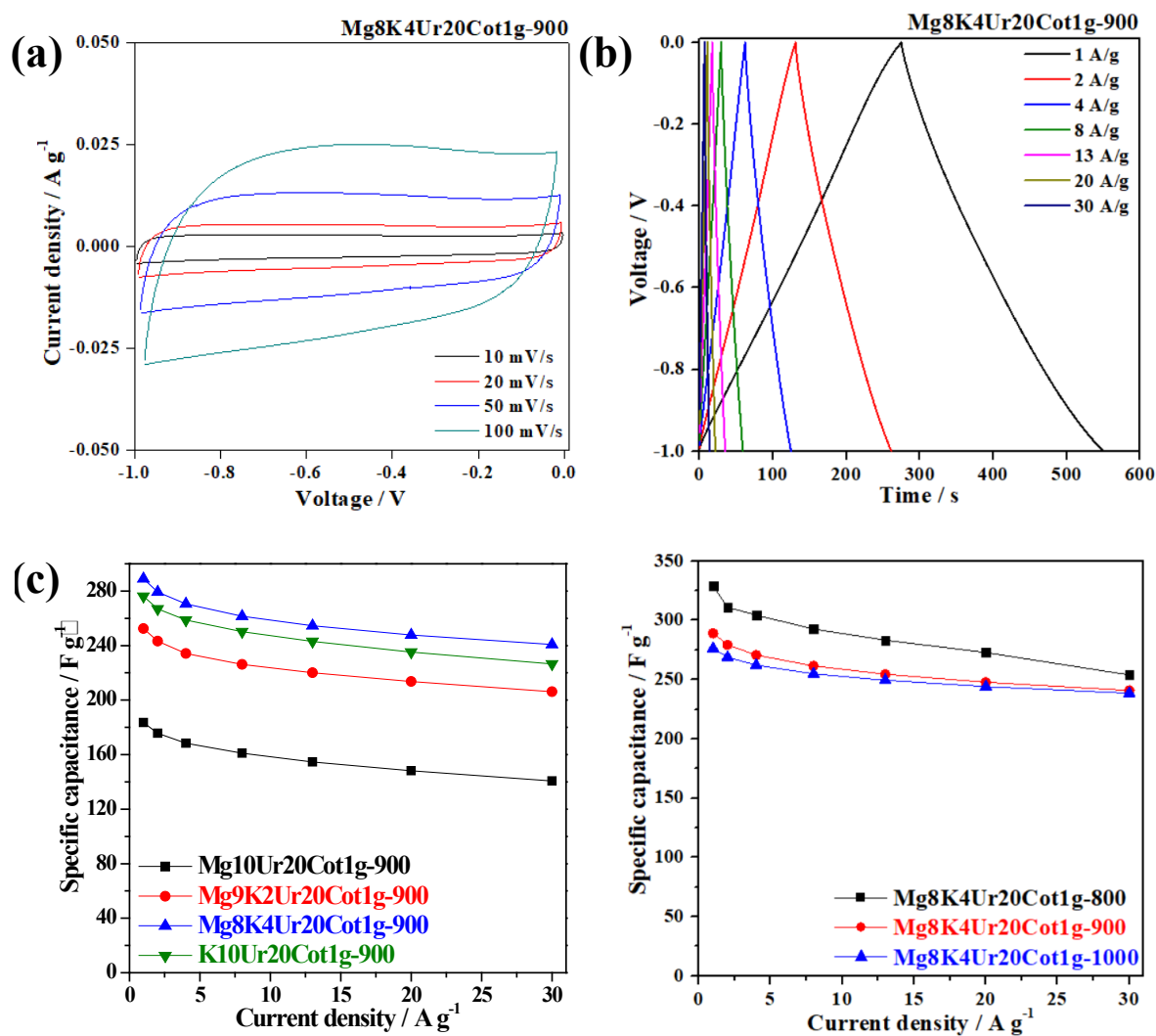


Figure 9. Three-electrode test of the supercapacitors in 6 mol L⁻¹ KOH. (a) Cyclic voltammogram curves of the Mg8K4Ur20Cot1g-900 at various scan rates. (b) Galvanostatic charge-discharge curves of Mg8K4Ur20Cot1g-900 under various current densities. (c, d) Specific capacitance at various current density.

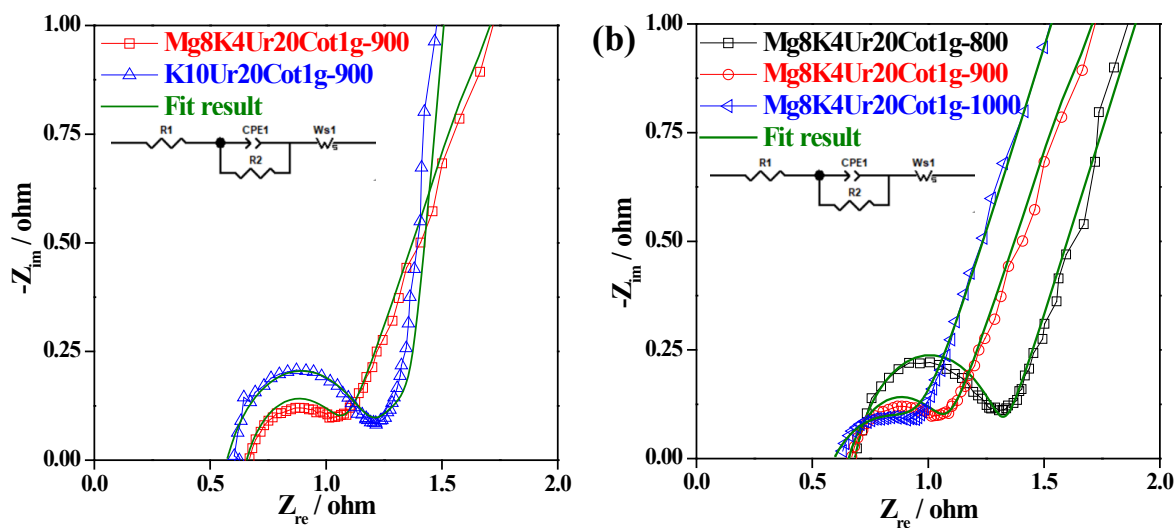


Figure 10. Typical Nyquist plots of the supercapacitors in 6 mol L⁻¹ KOH after CV measurement. (a) The samples with typical different pore size distribution; (b) the samples with different carbonization temperature.

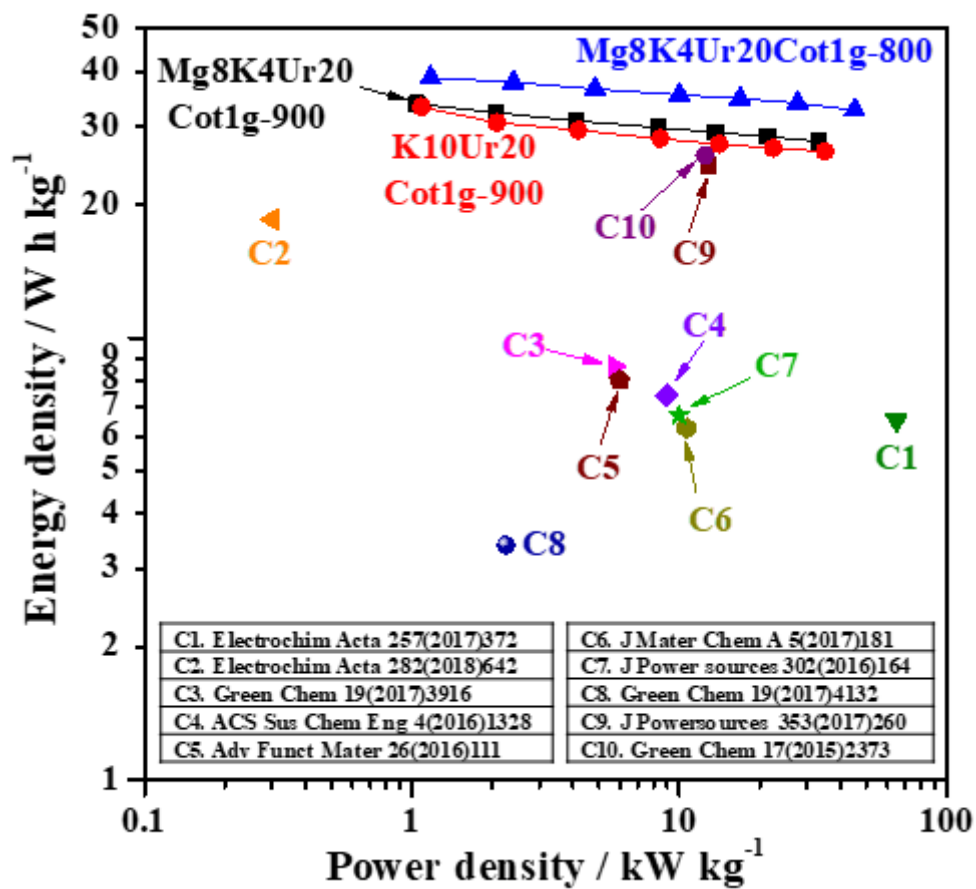


Figure 11. The Ragone plots showing energy and power densities of Mg8K4Ur20Cot1g-900, K10Ur20Cot1g-900, and Mg8K4Ur20Cot1g-800 in 6 M aqueous KOH electrolytes in comparison with previously reported data.

Table 1. Summary of the porous characteristics for porous carbon products obtained after acid washing.

	BET SSA (m ² g ⁻¹)	a _{total} (m ² g ⁻¹)	a _{ex} (m ² g ⁻¹)	a _{mi} cro=a _{total} - a _{ex} (m ² g ⁻¹)	V _{0.99} (cm ³ g ⁻¹)	V _{0.95} (cm ³ g ⁻¹)	V _{micro} (cm ³ g ⁻¹)	V _m eso =V _{0.95} -V _{micro} (cm ³ g ⁻¹)
Mg10Ur20 Cot1g-900	1102	1073	468	605	2.10	1.31	0.48	0.83
Mg9K2Ur20 Cot1g-900	2071	2217	350	1867	2.18	1.47	0.84	0.63
Mg8K4Ur20 Cot1g-800	2743	2407	372	2035	2.68	2.04	1.38	0.64
Mg8K4Ur20 Cot1g-900	2600	2355	386	1969	2.52	1.83	1.17	0.66
Mg8K4Ur20 Cot1g-1000	2774	2564	321	2243	2.44	1.90	1.34	0.56
K10Ur20 Cot1g-900	2486	2480	83	2397	1.43	1.30	1.16	0.14

BET SSA: specific surface area as-calculated from the adsorption data by BET method; V_{0.99}: total pore volume at P/P₀=0.99, corresponding to the pores with diameters up to around 200 nm; V_{0.95}: total pore volume at P/P₀=0.95, corresponding to the pores with diameters up to around 40 nm; a_{total}: the total surface area as-determined by t method; a_{ex}: the external surface area as-determined by t method; a_{micro}: the micropore surface area as-determined by a_{total}-a_{ex}; V_{micro}: the micropore volume as-analyzed by t method; V_{meso}: the mesopore volume as-determined by V_{0.95}-V_{micro}.

Table 2. Summary of the chemical bonding properties of the carbon samples obtained by XPS and Raman analysis.

<i>Samples</i>	<i>N content</i> [at. %]	<i>Percentage of N species</i>			<i>I_D/I_G</i> ratio from Raman
		Graphitic	Pyrrolic	Pyridinic	
		(~401.3 ev) [%]	(~400.0 ev) [%]	(~398.5 ev) [%]	
Mg10Ur20Cot1g-900	4.1	31.6	32.2	36.2	1.27
Mg9K2Ur20Cot1g-900	1.8	38.9	37.1	23.9	1.02
Mg8K4Ur20Cot1g-800	2.0	19.4	56.6	24.0	1.01
Mg8K4Ur20Cot1g-900	1.1	40.3	36.2	23.5	1.04
Mg8K4Ur20Cot1g-1000	0.8	48.8	34.1	17.1	1.05
K10Ur20Cot1g-900	0.7	41.4	35.5	23.0	0.99